RSC Advances

PAPER

View Article Online
View Journal | View Issue

Cite this: *RSC Adv.*, 2020, **10**, 15870

A new Bi_2MoO_6 nano-tremella-based electrochemical immunosensor for the sensitive detection of a carcinoembryonic antigen†

Zhongmin Wang,[a] Xinli Tian,[a] Dong Sun,[b] Penghui Cao,[a] Mengkui Ding,[a] Yuhao Li,[a] Ning Guo,[a] Ruizhuo Ouyang *[a] and Yuqing Miao[a]

By doping molybdenum (Mo) into bismuth oxide (Bi_2O_3), we synthesized novel Bi_2MoO_6 nanohybrids with a unique tremella-like crystal structure *via* a one-pot hydrothermal method. Such a porous tremella structure of Bi_2MoO_6 possesses a significantly larger surface area than the spherical structure of Bi_2O_3, which is favorable for the special functionalization and effective immobilization of molecules such as antibodies on the surface of the tremella flaps. As expected, Au nanoparticles grew easily and uniformly outside the surface of the flaps of the as-prepared Bi_2MoO_6 NTs (Au@Bi_2MoO_6 NTs), showing preferable conductivity and biocompatibility, and the anti-carcinoembryonic antigen (anti-CEA) was effectively immobilized outside the obtained Au@Bi_2MoO_6 NTs. Acting as a novel label-free immunosensing platform, the anti-CEA-immobilized Au@Bi_2MoO_6 NTs were used to fabricate an electrochemical immunosensor for the quantitative detection of CEA. The as-prepared Au@Bi_2MoO_6-based immunosensor linearly responded to CEA in a wide concentration range from 1 pg mL^{-1} to 1 μg mL^{-1} with a detection limit calculated to be 0.3 pg mL^{-1} (S/N = 3), significantly comparable to numerous existing immunosensors. Moreover, the minimum detection concentration of the designed immunosensor was about ten times smaller than that of many Bi and Mo-based sensors toward CEA detection, and the detection limit was lower, revealing higher sensitivity. The satisfactory selectivity and stability made the immunosensor potentially applicable for CEA detection in real samples.

Received 28th February 2020
Accepted 2nd April 2020

DOI: 10.1039/d0ra01922d

rsc.li/rsc-advances

1. Introduction

Cancer is the most common type of malignancy without obvious non-specific symptoms in the early stage of malignant tumors.[1,2] We are far from blocking the pace of cancer despite numerous progress achieved in cancer research over the years. However, early diagnosis of cancer can significantly improve the cure and survival rate.[3,4] Common cancer screening methods include genetic testing, imaging examination, endoscopy, pathological examination, and tumor marker detection.[5] Tumor marker detection is the most effective and potential means of detecting cancer at an early stage, which is mainly carried out *via* enzymatic examination. For example, liver cancer and lung cancer can be significantly screened by detecting alkaline phosphatase and glycoproteins, respectively. The occurrence of liver cancer and malignant teratoma can result in an increase in alpha-fetoprotein (AFP).[6] Lung, colorectal and breast cancer can be diagnosed and evaluated early by detecting the concentration of carcinoembryonic antigen (CEA).[7–10] Therefore, the quick and sensitive detection of tumor markers is significantly important for the early diagnosis and treatment of cancer.

In recent years, electrochemical immunosensors have received considerable attention due to their numerous advantages such as simplicity, sensitivity, and low cost.[11] Voltammetric immunosensors usually use an electrolyte solution containing reversible redox species such as ferricyanide ($[Fe(CN)_6]^{3-/4-}$) for good reversible oxidation–reduction.[12] On the other hand, unlabeled voltammetric immunosensors are fabricated by dropping the redox substance on the electrode surface to bind the antibody through chemical bonds, thereby eliminating the direct contact of the electrode with the antibody.[12] The key of this approach is the selection of the material modifying the electrode so as to accelerate electron transfer and amplify the signal. Therefore, numerous materials were chosen to improve the sensitivity of the immunosensor. For example, graphene oxide is widely used because of its low cost, large specific surface area, excellent mechanical properties, good electronic properties and excellent thermal properties.[7,13–15] Apart from this, mesoporous silica (SiO_2),[16] photoactive conducting poly(5-formylindole) nanocomposites,[17] magnetic nanomaterials (Fe_2O_3, Fe_3O_4, *etc.*),[18,19] ceria (CeO_2),[20] cuprous

[a]*Institute of Bismuth Science, The University of Shanghai for Science and Technology, Shanghai 200093, China. E-mail: ouyangrz@usst.edu.cn*

[b]*School of Chemistry and Chemical Engineering, Henan Normal University, Xinxiang 453007, China*

† Electronic supplementary information (ESI) available. See DOI: 10.1039/d0ra01922d

oxide (Cu_2O)[21] and platinum (Pt)[22] are commonly used for electrode modification.

Usually, the materials with poor biocompatibility can inevitably cause toxicity, irritation, teratogenicity, and local inflammation of cells and the whole body, after undergoing a short-term contact, while the long-term contact may exert mutagenic, teratogenic and even carcinogenic effects. Also, the transportation of such materials through blood may cause abnormal coagulation function and hemolysis. Therefore, biocompatibility is a significantly important indicator to be evaluated for materials used in biological applications, including biosensors.[23,24] Until now, the application of bismuth (Bi)-based nanomaterials in biosensors has attracted increasing attention due to their good stability in nature and extremely low toxicity to the body. For instance, Han used the cerium-doped CdS-sensitized $BiYWO_6$ to detect tetracycline, reducing the detection limit to 0.01 ng mL^{-1} with good stability.[25] Wu *et al.* developed a label-free photoelectrochemical (PEC) immunosensor based on CdS nanowires sensitized with a WO_3@BiOI heterostructure for CEA detection with good stability and high sensitivity.[26] An Ag ion-modified bismuth vanadate nanopolyhedron ($BiVO_4$@Ag^+) was utilized as a label to immobilize anti-AFB1 through affinity specific binding.[27] Among those Bi-based materials, Bi_2O_3 is an important semiconductor material because of its narrow band-gap (about 2.8 eV), relatively high power and capacity, and electrochemical stability.[28] The Bi_2O_3 nanoparticles (NPs) synthesized *via* a hot solvent method have good photocatalytic performance.[29] Also, polycrystalline Bi_2O_3 was used to construct a new nano-bio-based amperometric glucose biosensor,[30] and Bi_2O_3 nanorods were produced to modify an indium–tin-oxide electrode for the quantitative detection of mycotoxin,[31] revealing the good biocompatibility of Bi_2O_3. However, the conductivity of Bi_2O_3 is not good enough and somehow limits its application in an electrochemical analysis. Moreover, molybdenum (Mo) containing nanomaterials have received considerable attention in recent years due to their good biocompatibility and high metallic-like electrical conductivity. The palladium NP-functionalized three-dimensional wrinkly amorphous MoS_x composites were used as an electrochemical immunosensing platform to determine insulin.[32] The hierarchically 1D MoO_2 particles exhibited remarkable electrocatalytic activity with good long-term cycle stability for the hydrogen evolution reaction (HER) in acidic media.[33] An amino-functionalized coral-like MoS_2@Cu_2O hybrid with increased surface area and conductivity was used to amplify the signal.[34] Gao successfully developed Au@Pd/MoS_2-modified multi-walled carbon nanotubes (MWCNTs) to improve high specific surface area and good biocompatibility.[35]

Usually, Bi_2O_3 shows a spherical or nanowire structure[28,36] with a relatively small specific surface area and low electron transfer rate, which is not favorable for the amplification of electrical signals, the effective immobilization of biomolecules and even the deposition of other NPs. In this study, Mo was doped into Bi_2O_3 to prepare a Bi-based hybrid material (Bi_2MoO_6) *via* a one-pot hydrothermal method. As expected, the spherical structure of Bi_2O_3 was changed to a porous tremella-like structure (Bi_2MoO_6 NTs) with a large surface area by incorporating Mo into Bi_2O_3, which is beneficial for the metal NPs to grow and the antibody to bind on the flap surface of the Bi_2MoO_6 NTs specifically. By comparison, both the electron transfer and biocompatibility of Bi_2MoO_6 NTs were significantly improved, which was favorable for the fabrication of an electrochemical immunosensor. As expected, Au NPs easily grew on the flaps of Bi_2MoO_6 NTs (Au@Bi_2MoO_6 NTs), further enhancing the electron transfer performance and biocompatibility of the hybrid Bi_2MoO_6 NTs. To the best of our knowledge, it is the first time to synthesize tremella-like Bi_2MoO_6 nanohybrid and use it as an electrochemical immunosensing platform to detect CEA, where the excellent analytical performance was achieved toward CEA detection. Scheme 1 illustrates the preparation of the Bi_2MoO_6 NT-based electrochemical immunosensor toward CEA detection.

2. Experimental

2.1. Reagents

The antibody of CEA (anti-CEA), CEA, prostate-specific antigen (PSA), immunoglobulin G (IgG), albumin from bovine serum (BSA) and AFP were purchased from Shanghai Linc-Bio Science Co. Ltd (Shanghai, China). Barium nitrate pentahydrate ($Bi(NO_3)_3\cdot 5H_2O$), concentrated HNO_3 (65–68%), polyvinylpyrrolidone (PVP), NaOH (99.99%), ethylene glycol (EG, >99%), glutaraldehyde (GA), CTAB, potassium hexacyanoferrate(II) trihydrate ($K_4Fe(CN)_6$), potassium hexacyanoferrate(III) ($K_3Fe(CN)_6$), sodium borohydride ($NaBH_4$), sodium citrate, chloroauric acid ($HAuCl_4$), trisodium citrate dihydrate ($Na_3C_6H_5O_7\cdot 2H_2O$), potassium chloroaurate ($KAuCl_4$), ascorbic acid (AA), 3-aminopropyl)triethoxysilane (APTES), disodium phosphate (Na_2HPO_4) and sodium dihydrogen phosphate(NaH_2PO_4) were obtained from Aladdin Industrial Corporation (Shanghai, China). Molybdenum acetylacetonate (($MoO_2(acac)_2$) was provided by Tansoole (Shanghai, China). All other chemicals were of analytical reagent grade and used without any further treatment. Deionized water and absolute ethanol were used throughout the experiment.

2.2. Apparatus

Scanning electron microscopy (SEM) measurements were performed on an FEI QUANTA FEG250 coupled to an INCA Energy X-MAX-50. X-ray photoelectron spectroscopy (XPS) measurements were carried out using a single-color AlKα source with ESCALAB 250 XI. UV-Vis absorption spectra were recorded on a UV-Vis 1901 spectrophotometer (Phoenix). All electrochemical measurements were accomplished on a CHI660D workstation (Chenhua Instrument Shanghai Co., Ltd, China). X-ray diffraction (XRD) were obtained on a Rigaku Ultimate IV (Rigaku, Japan).

2.3. Preparation of the Bi_2O_3 nanocrystals

0.182 g of $Bi(NO_3)_3\cdot 5H_2O$ was dissolved in 5 mL 1.0 mol L^{-1} HNO_3 solution, immediately followed by the addition of 0.064 g NaOH, 0.6 g PVP and 25 mL EG. The obtained solution was then transferred to a 50 mL Teflon reactor, which was sealed in

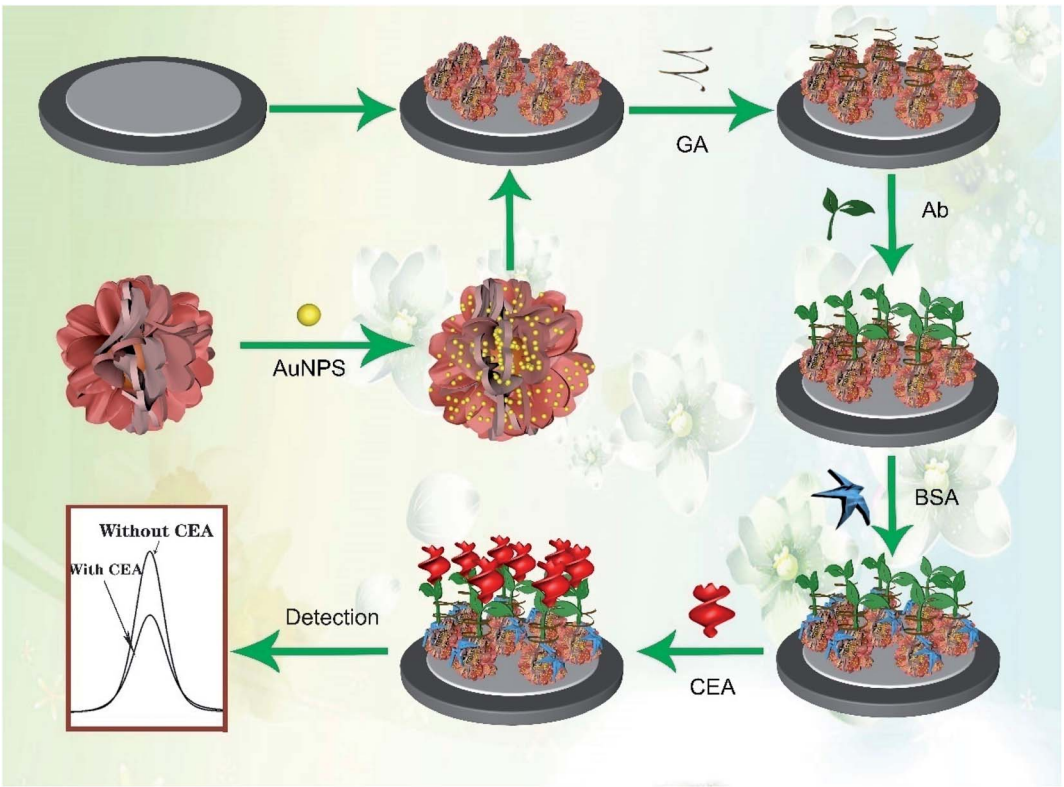

Scheme 1 Schematic of the preparation of the Bi_2MoO_6 NT-based electrochemical immunosensor toward CEA detection.

a stainless steel autoclave and heated at 150 °C for 3 h. The cooled solution was centrifuged at 10 000 rpm for 10 min to collect Bi_2O_3 NPs, which were then thoroughly washed and freeze-dried for use.[36]

2.4. Preparation of the MoO_2 nanocrystals

Typically, 0.08 g $MoO_2(acac)_2$ was gradually dissolved in 20 mL of a mixed solution containing absolute ethanol and 5 mL deionized water in a molar ratio of 3 : 1 under stirring. After stirring for 2 h, the solution was heated to 180 °C and kept for 10 h. Next, the solution was cooled to room temperature and then centrifuged to obtain the precipitate of MoO_2 nanocrystals, which was washed with ethanol several times and freeze-dried for subsequent use.[37]

2.5. Preparation of the Bi_2MoO_6 NTs

The Bi_2MoO_6 NTs were prepared *via* a one-pot synthesis method. First, 0.05 g Bi $(NO_3)_3 \cdot 5H_2O$ was dissolved in 20 mL absolute ethanol and stirred for 1 h. Then, 0.08 g $MoO_2(acac)_2$ was added into the solution, followed by 1 h stirring. Next, 0.5 g CTAB was successively dissolved in the mixture. After stirring for 1 h, the solution was transferred into a Teflon-lined stainless-steel autoclave for 12 h at 160 °C. Bi_2MoO_6 NTs were finally obtained by centrifuging the solution at 10 000 rpm for 10 min, which were then washed with ethanol and ultrapure water three times and dried in a drying oven at 60 °C for 8 h.

2.6. Amino functionalization of Bi_2MoO_6 NTs and preparation of gold seeds

0.012 g Bi_2MoO_6 NTs were dispersed into 30 mL absolute ethanol, followed by the addition of 1.0 mL of ATPES under stirring. After 3 h of stirring, the solution was refluxed at 70 °C for 1.5 h under stirring for the amino functionalization. Finally, the solution was centrifuged at 10 000 rpm for 5 min to collect the NH_2 group-functionalized Bi_2MoO_6 NTs (Bi_2MoO_6–NH_2), which were dispersed in 15 mL absolute ethanol for subsequent use.

A solution of gold seeds was prepared based on a previously reported method.[38] Briefly, 200 μL of a 10 mM $HAuCl_4$ solution was added into 10 mL of deionized water, and 200 μL of 10 mM trisodium citrate was then rapidly added in under stirring. 10 min later, 200 μL of a 100 mM $NaBH_4$ solution was pipetted into the mixture, which was stirred for 30 min till the solution color changed to red.

2.7. Modification of Bi_2MoO_6 NTs with Au NPs

First, 1.0 mL of the above prepared Bi_2MoO_6–NH_2 NTs was ultrasonically dispersed in 10 mL of absolute ethanol. Then, a 60 μL gold nanoseed-containing solution was subsequently added under stirring, immediately followed by the addition of a 300 μL 10 mM $HAuCl_4$ solution. Second, 300 μL of 10 mM sodium citrate was added into the mixed solution. After the solution was stirred for 5 min, 100 μL 0.1 M AA was pipetted into the mixed solution to allow the growth of Au NPs for 30 min.

Finally, the resultant product was centrifuged repeatedly at 10 000 rpm for 10 min with ethanol. After being dried in an oven at 60 °C for 8 h, the final Au NP-modified Bi_2MoO_6 NTs (Au@Bi_2MoO_6 NTs) were stored at room temperature for subsequent use. The schematic of the synthetic material is fully illustrated in Scheme 2.

2.8. Immunoassay of CEA based on Au@Bi_2MoO_6 NTs

After the bare GCE was polished with 0.3 μm and 0.05 μm alumina slurry, respectively, and dried at room temperature, a certain amount of Au@Bi_2MoO_6 NTs was dropped onto the electrode surface. 0.2 mM GA (2.5%) was dropped on the Au@Bi_2MoO_6 NT-modified GCE at 30 °C for 1 h as a cross-linker to connect anti-CEA. Afterward, 6 μl of 75 ng mL^{-1} anti-CEA was dropped on the surface of the functionalized electrode and incubated at 30 °C for 1 h, followed by washing with PBS and air-drying at 30 °C. Then, 6 μL BSA (1%) was pipetted on the surface of the anti-CEA immobilized electrode surface and incubated for 60 min to cover the inactive sites. After being washed with PBS and air-dried sequentially, the Au@Bi_2MoO_6 NT-based electrochemical immunosensor was finally obtained and stored at 4 °C for CEA detection. Scheme 1 shows the fabrication of the Au@Bi_2MoO_6 NT-based immunosensor toward CEA detection.

2.9. Electrochemical measurements

All the electrochemical measurements were carried out in the solution of PBS (pH = 6.5) containing 5 mM $[Fe(CN)_6]^{3-/4-}$ and 0.1 M KCl through a three-electrode system using a differently modified glassy carbon electrode (GCE, d = 3 mm), a platinum wire and a silver/silver chloride (Ag/AgCl) as the working, auxiliary and reference electrodes, respectively. The cyclic voltammetries (CV) were obtained in the scanning potential range from −0.2 to 0.8 V at a sweep speed of 0.1 V s^{-1}. The square wave voltammetry plots were performed in the scan range from 0.0 to 0.6 V. The electrochemical impedance spectroscopy (EIS) was scanned from 0.01 to 100000 Hz (amplitude: 0.005 V, quiet time: 2 s). Before the detection, the as-prepared Au@Bi_2MoO_6 NT-based immunosensor was incubated with CEA at different concentrations at 30 °C for 60 min. Right after the immune combination between anti-CEA and CEA, the electrodes were washed with PBS to remove the unbound CEA.

3. Results and discussion

3.1. Characterizations of Bi_2MoO_6 NTs and Au@Bi_2MoO_6 NTs

3.1.1 SEM and XRD analysis. By comparison, both Bi_2O_3 and MoO_2 were synthesized, showing a spherical shape with a particle size of about 300 nm (Fig. 1A and B). After Mo and Bi were mixed to prepare the hybrid, the morphology of the hybrid changed greatly, from the original sphere to a tremella-like nanostructure (Fig. 1C and D, the inset is a photo of real tremella). Although the particle size (950–1000 nm) increased, the surface area of the obtained porous Bi_2MoO_6 NTs was greatly enlarged due to the formation of a tremella structure. The change in morphology indicated that the two elements were not simply mixed, but formed a nanohybrid. More importantly, such a porous tremella nanostructure is good for the further surface modification of Bi_2MoO_6. Fig. S2† shows the XRD patterns of the as-prepared Bi_2MoO_6 and pure Bi_2O_3. The peaks from left to right correspond to (131), (002), (210), (212), (260), (331), (133) and (391) of Bi_2MoO_6 (JCPDS no. 84-0787), a single orthorhombic crystal, confirming the successful preparation of the Bi_2MoO_6 hybrid crystal. In addition, Au NPs with an average diameter of 50 nm were easily and uniformly decorated on the flap surface of Au@Bi_2MoO_6 NTs as expected (Fig. 1E and F).

Moreover, the mapping analysis of Au@Bi_2MoO_6 NTs indicated that the metals of Bi, Mo and Au were uniformly distributed throughout Au@Bi_2MoO_6 NTs (Fig. 2), verifying the successful synthesis of the Bi_2MoO_6 nanohybrid and the uniform distribution of Au NPs on the flap surface of Bi_2MoO_6 NTs.

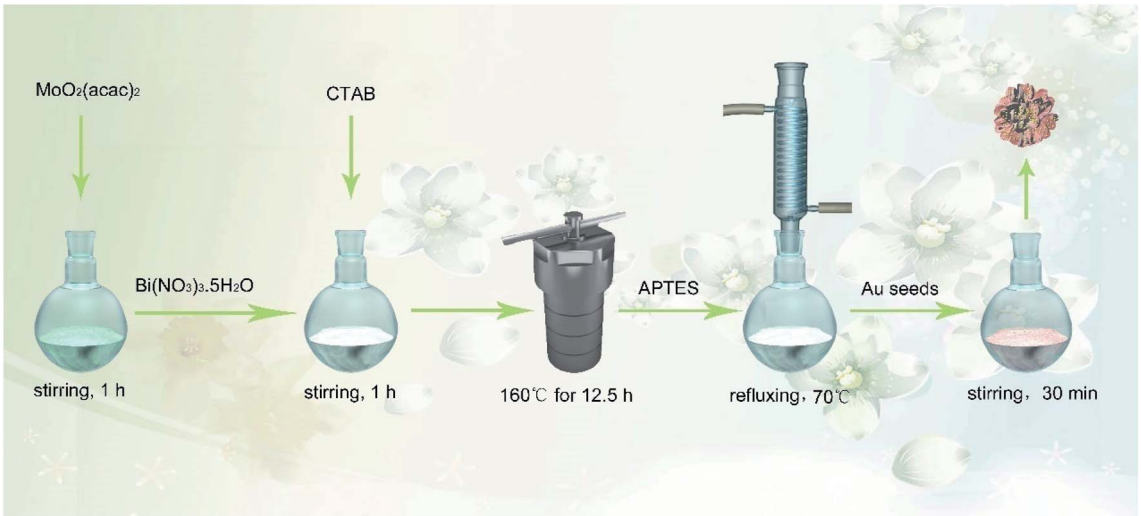

Scheme 2 The schematic for the synthesis of Au@Bi_2MoO_6 NTs.

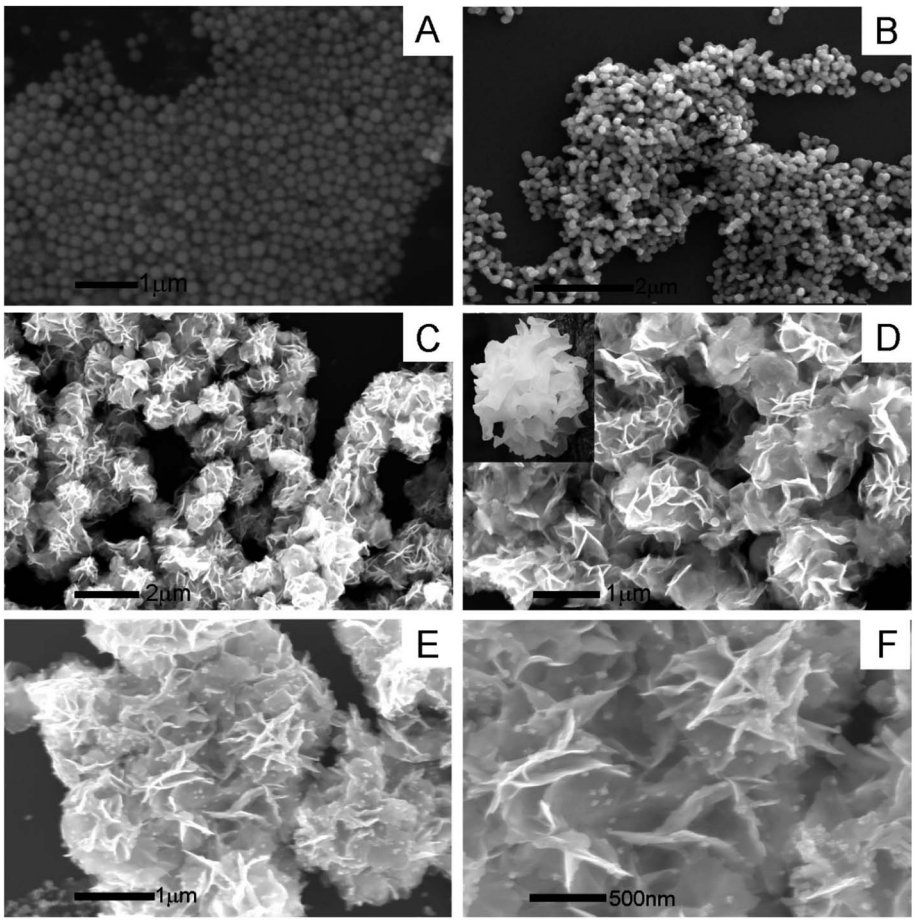

Fig. 1 SEM images of (A) Bi_2O_3, (B) MoO_2, (C and D) Bi_2MoO_6, and (E and F) Au@Bi_2MoO_6 in different magnification scales.

3.1.2 XPS and UV characterizations. XPS was also performed to determine the elemental composition of the as-prepared Au@Bi_2MoO_6 NTs, as shown in Fig. 3. The binding peaks of Mo, Bi, O and Au elements are observed in the survey spectrum (Fig. 3A), confirming their coexistence inside the Au@Bi_2MoO_6 NTs. In the fitted spectrum of Mo3d (Fig. 3B), the two peaks at 235.05 eV and 235.1 eV correspond to the binding between Mo and O. The Bi–O bond is reflected by the presence of a binding peak at 164.15 eV and 158.85 eV, as shown in Fig. 3C, the fitted spectrum of Bi4f.[39] Also, the binding of O with both Bi and Mo was proved by the presence of a peak at 531.95 eV in the O1s fitted spectrum (Fig. 3E). All the results were indicative of the successful formation of Bi_2MoO_6 NTs. In addition, in Fig. 3D, the Au4f spectrum represented the XPS signature of the Au4f doublet ($4f^{5/2}$ and $4f^{7/2}$) at 87.00 eV and 83.35 eV, suggesting the presence of Au NPs in Bi_2MoO_6 NTs. Fig. 3F shows the UV-vis absorption spectra of Bi_2MoO_6 NTs before and after the modification of Au NPs. By comparison, a strong absorption peak at 570 nm is observed for Bi_2MoO_6 NTs after Au NPs grew outside, further confirming the formation of Au NPs on Bi_2MoO_6 NTs.

3.1.3 Properties of electron transfer and biocompatibility. Fig. 4A and B show the CV and EIS plots of bare GCE and GCEs modified with Bi_2O_3, MoO_2, Bi_2MoO_6 and Au@Bi_2MoO_6 NTs, respectively. After the modification of Bi_2O_3, the current slightly decreased and the semi-circle clearly increased compared with the bare GCE, revealing the poor conductivity of Bi_2O_3. As expected, the incorporation of Mo into Bi_2O_3 enhanced the electron transfer rate of Bi_2MoO_6 NTs, indicating the good conductivity of Bi_2MoO_6 NTs, which was likely caused by the lattice occupancy of Mo inside the Bi_2O_3 crystal structure, and the decoration of Au NPs further improved the conductivity of Bi_2MoO_6 NTs, preferred for the fabrication of the electrochemical immunosensor.

Both contact angle and toxicity toward 4T1 cells were tested to explore the hydrophilicity and biocompatibility of Au@Bi_2MoO_6 NTs (Fig. 4C and D). As shown in Fig. 4C, the initial contact angle of Au@Bi_2MoO_6 NTs was 33.7–34.8°, showing favorable hydrophilicity. The modification of GA further reduced the contact angle to 20.4–21.6°, revealing better hydrophilicity, which is helpful for the immobilization of biomolecules, and the contact angle continued to decrease to 14.3–15.1° after the Au@Bi_2MoO_6 NT-modified GCE was incubated with anti-CEA, revealing the successful immobilization of anti-CEA on Au@Bi_2MoO_6 NTs.

Fig. 4D shows the cellular activity of the 4T1 cells treated with Au@Bi_2MoO_6 NTs at different concentrations. Clearly, Au@Bi_2MoO_6 NTs did not affect the viability of the 4T1 cells

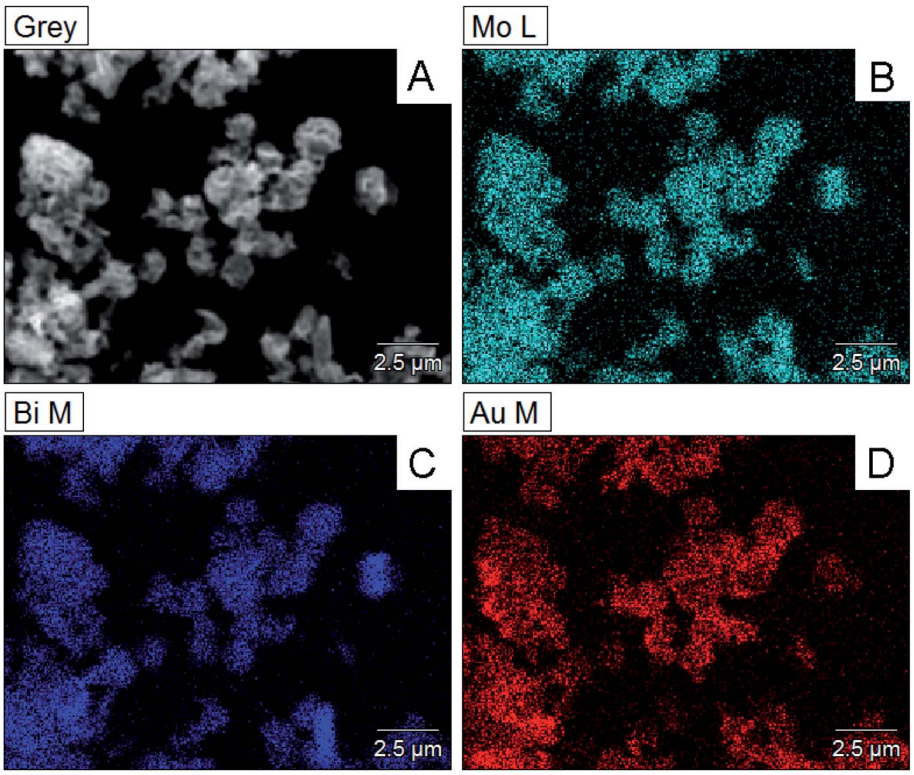

Fig. 2 The mapping analysis of (A) Au@Bi_2MoO_6; and elements of (B) Mo, (C) Bi and (D) Au.

even when the concentration of Au@Bi_2MoO_6 NTs reached 200 ppm. These results indicate the high biocompatibility and low cytotoxicity of Au@Bi_2MoO_6 NTs.

3.2. Electrochemical behaviors of the Bi_2MoO_6@Au NT-based immunosensor

The CVs of the as-prepared Bi_2MoO_6@Au NT immunosensor were carried out in 5.0 mM $[Fe(CN)_6]^{3-/4-}$ containing 0.1 M KCl (pH = 6.5) at different scan rates to study the electrochemical process. As demonstrated in Fig. 5A, the peak current (I) was dependent on the scan rate: both the anodic and cathodic peak currents increased with the increase in the scan rate from 10 to 400 mV s^{-1} and were directly proportional to the square root of the scan rate ($\nu^{1/2}$), as shown in Fig. 5B, revealing that the electrochemical process of the as-prepared Bi_2MoO_6@Au NT-based immunosensor was controlled by diffusion.

DPV plots of differently modified GCEs were obtained to verify the successful layer-by-layer preparation (Fig. 5C). As can be seen, the Au@Bi_2MoO_6 TN-modified GCE (curve a) shows the highest current peak, which decreased after Ab was immobilized (curve b). BSA was used to cover the non-specific site on the electrode surface, which led to a further current decrease (curve c). The incubation of Au@Bi_2MoO_6-Ab-BSA with CEA continuously reduced the current, confirming the successful immobilization of CEA (curve d). The decreased in current can be attributed to the deposited proteins, which may prevent the interfacial electron transfer and reduce the active sites accessible to ferricyanide,[40] verifying the successful layer-by-layer modification of biomolecules on the Au@Bi_2MoO_6 NT-modified electrode. Fig. 5D compares the response signal of the Au@Bi_2MoO_6 NT-based immunosensor before and after the immobilization of CEA. A sensitive response to CEA was observed using the as-prepared immunosensor.

3.3. Analytical performance, reproducibility and selectivity

As discussed above, a label-free immunosensor was designed based on Au@Bi_2MoO_6 NTs that directly converted the competitive immune response into measurable electrochemical signals. In order to achieve the best analytical performance of the Au@Bi_2MoO_6 NT-based immunosensor toward CEA detection, the experimental conditions were well optimized, which included the concentration of Au@Bi_2MoO_6 NTs, the pH of PBS, the concentration of anti-CEA and the antibody–antigen reaction (see the ESI S2 and Fig. S2†). Under the optimal conditions, the analytical performance with SWV of the Au@Bi_2MoO_6 NT-based immunosensor was examined toward CEA at different concentrations. As shown in Fig. 6A and B, the peak current was proportionally weakened as the concentration of CEA increased owing to the binding of more CEA molecules to anti-CEA on the electrode surface (Fig. 6A). A linear relationship between the peak current (I) and the logarithm of the CEA concentration (c) was achieved from 1 pg mL^{-1} to 1000 ng mL^{-1}, where an equation of $I = 96.791 - 6.0913 \lg c$, was obtained with the correlation coefficient and limit of detection (S/N = 3)

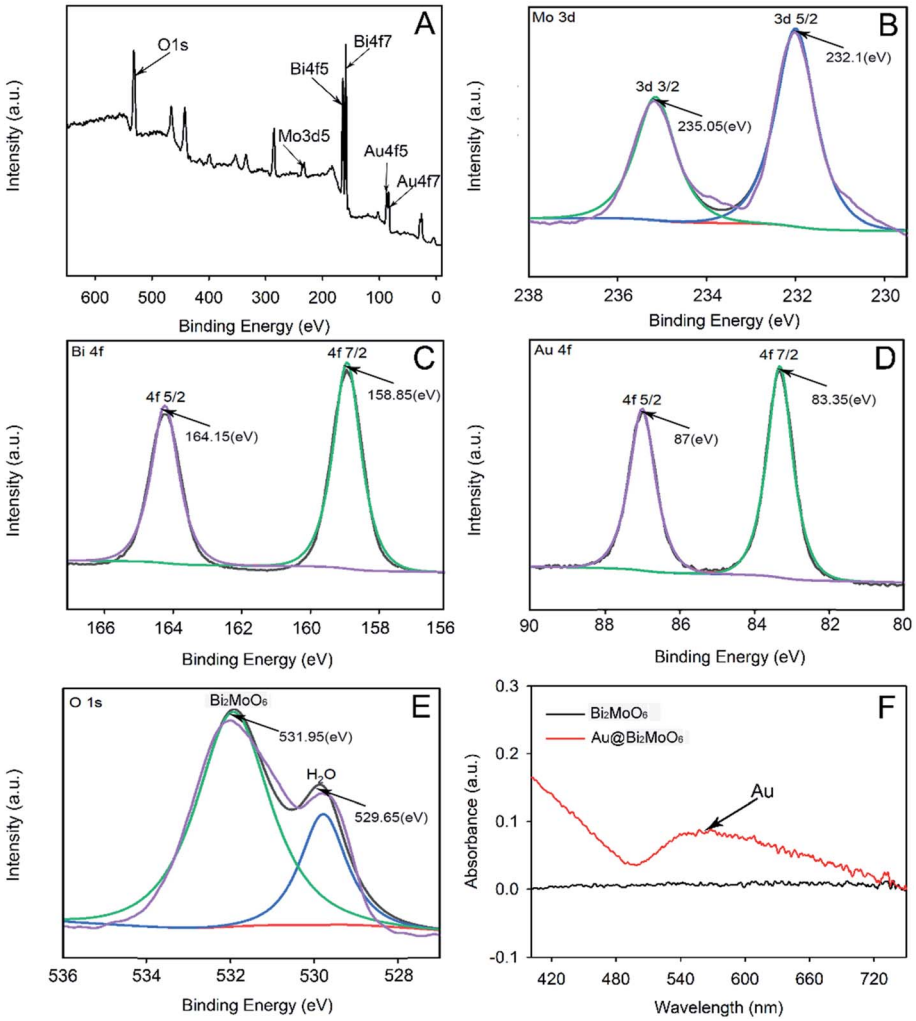

Fig. 3 XPS spectra of the Bi_2MoO_6 NTs. (A) Survey spectrum of Bi_2MoO_6 NTs and the fitted spectra of (B) Mo3d, (C) Bi4f, (D) Au4f, (E) O1s. (F) UV spectra of Bi_2MoO_6 NTs and Au@Bi_2MoO_6 NTs.

calculated to be 0.9976 and 0.3 pg mL^{-1}, respectively (Fig. 6B). The concentration of CEA in healthy adults is usually below 2.5 ng mL^{-1} and higher than 20 ng mL^{-1} in bodies at risk of cancer. However, the concentration of CEA varies between cancers. For example, the low level of CEA in colon tissue was reported to be 2.5–5.0 μg L^{-1}, but could greatly increase in patients with liver cancer.[7] Even so, the detection range of the designed immunosensor was sufficient to support the CEA detection in samples of various cancers with good sensitivity.

In addition, Table 1 compares the analytical behaviors of the current Au@Bi_2MoO_6 NT-based immunosensor with some other existing immunosensors toward CEA with respect to detection range and limit. The minimum detection concentration of the designed immunosensor was about ten times smaller than that of numerous existing immunosensors toward CEA detection, including Mo and Bi-based sensors, and the detection limit was lower, revealing higher sensitivity. Upon the comparison, a conclusion could be made that the Au@Bi_2MoO_6 NT-based immunosensor showed more comparable advantages in both detection range and detection limit, providing a promising alternative for CEA detection.

Five different electrodes were separately modified with Au@Bi_2MoO_6 NTs to fabricate the immunosensor so as to evaluate the reproducibility. Fig. 6C shows the response of the five individually prepared immunosensors to 1.0 ng mL^{-1} of CEA under the same conditions. It was found that no obvious difference in the peak current was observed among the five immunosensors with a relative standard deviation of 2.16%, revealing the satisfactory reproducibility of the designed Au@Bi_2MoO_6 NT-based immunosensor for CEA detection.

Moreover, IgG, PSA, AFP and BSA were selected to examine the specificity of the Au@Bi_2MoO_6 NT-based immunosensor for CEA detection (Fig. 6D). In the presence of each interferent at 100 ng mL^{-1}, the fabricated immunosensor did not show a significantly different response to 1 ng mL^{-1} CEA, and the detection behavior with the interfering substance present (100 fold higher) was not much different from that only with CEA, proving the satisfactory specificity of the present immunosensor, which is indicative of the preferable selectivity.

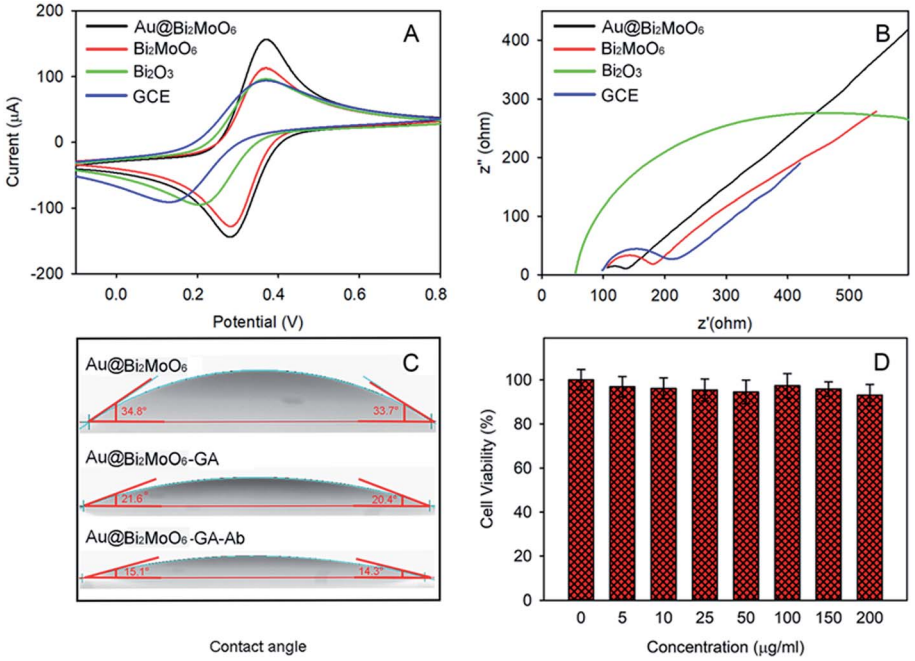

Fig. 4 (A) CV and (B) EIS plots of bare GCE and GCEs modified with Bi_2O_3, Bi_2MoO_6 and $Au@Bi_2MoO_6$ NTs, respectively; (C) contact angles of $Au@Bi_2MoO_6$ NTs, $Au@Bi_2MoO_6$-GA and $Au@Bi_2MoO_6$-GA-Ab; (D) cellular activity of 4T1 treated with $Au@Bi_2MoO_6$ NTs at different concentrations.

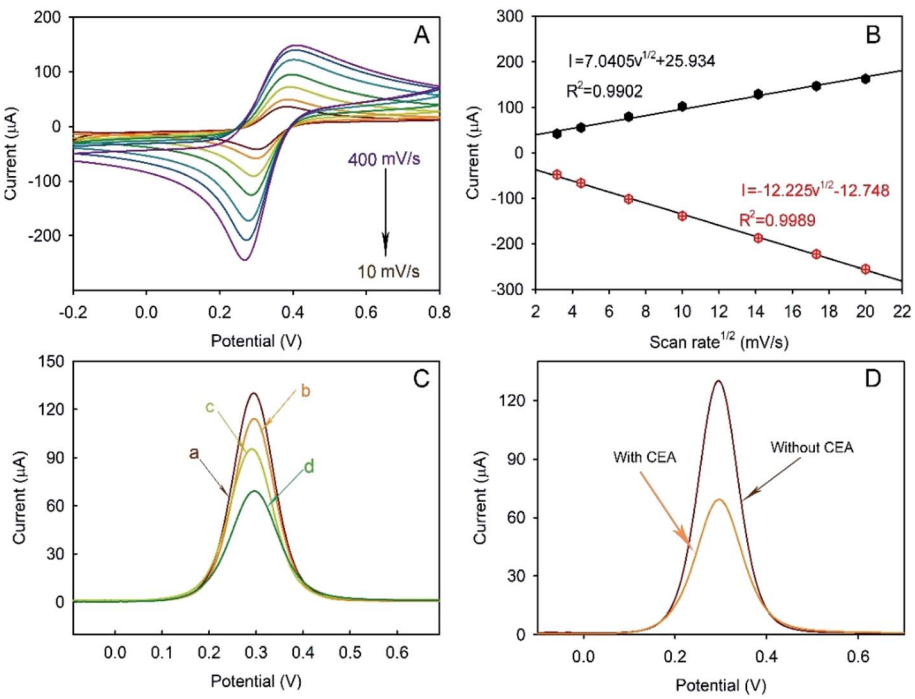

Fig. 5 (A) CVs of the proposed immunosensor at different scan rates (from outer to inner: 400, 300, 200, 100, 50, 20 and 10 mV s^{-1}); (B) the linear relationship between the square root of the scan rate and peak current; (C) voltammetric plots of GCEs modified with (a) $Au@Bi_2MoO_6$ NTs, (b) $Au@Bi_2MoO_6$-Ab, (c) $Au@Bi_2MoO_6$-Ab-BSA and (d) $Au@Bi_2MoO_6$-Ab-BSA-CEA; (D) DPV plots of $Au@Bi_2MoO_6$ NTs before and after the incubation of CEA.

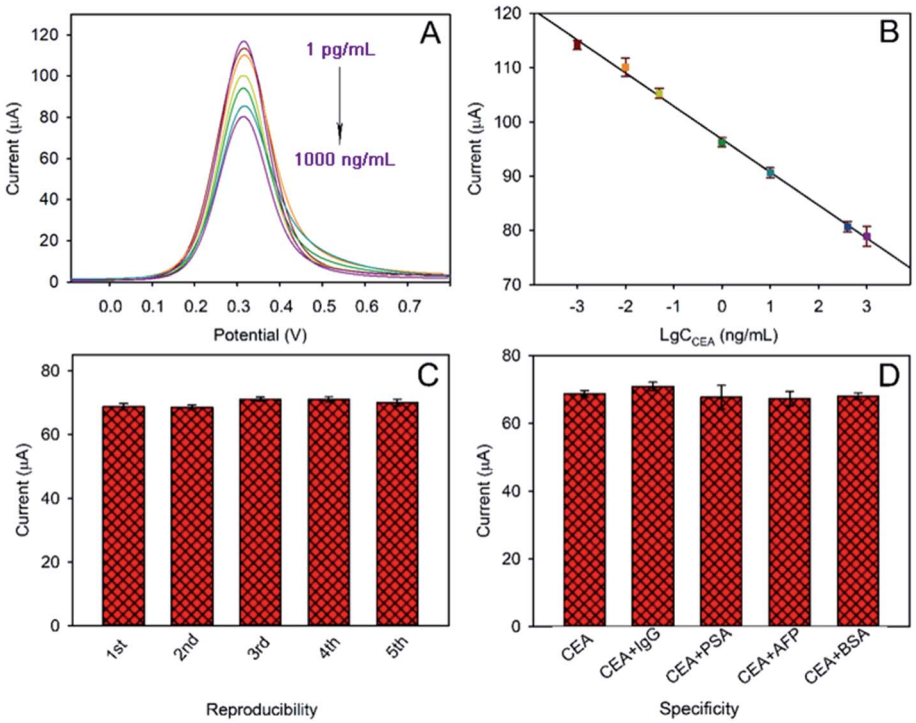

Fig. 6 (A) Voltammetric responses and (B) the calibration curve of the Au@Bi_2MoO_6 NT-based immunosensor to 0.001, 0.01, 0.05, 1, 10, 400 and 1000 ng mL^{-1} CEA in the solution containing 5 mM $[Fe(CN)_6]^{3-/4-}$ and 0.1 M KCl. (C) The reproducibility and (D) the specificity of the immunosensor.

Table 1 Analytical performances of different electrochemical immunosensors toward CEA detection[a]

Immunosensor	Linear range (ng mL^{-1})	Detection limit (pg mL^{-1})	Ref.
Cu-Au NP/CNT-CSs	0.025–25	0.5	41
3D-G/pDA/Con A	0.1–750	90	42
$Co_2(OH)_2CO_3$-CeO_2	0.002–75	0.51	43
Au-*g*-C_3N_4·NHs	0.02–80	6.8	44
AuNP/TiO_2-Gr/Thi/GCE	0.1–10.0	10	45
Au-PB-Fe_3O_4	0.01–80	4	46
AuNP/NBeERGO/GCE	0.001–40	0.45	7
AuNP/MWCNT/CS/GCE	0.3–2.5	10	47
MoS_2 nanosheets	0.1–100	34	48
Mo-Mn_3O_4/MWCNT/CS	0.1–125	4.9	8
I-BiOCl/CdS-10	0.01–40	2	49
Au@Bi_2MoO_6 NTs	0.001–1000	0.3	This work

[a] CNTs: carbon nano-tube arrays; CSs: carbon spheres; 3D-G: 3D graphene; pDA: polydopamine; Con A: concanavalin A; NHs: nanohybrids; PB: Prussian blue; NB-ERGO: Nile blue A hybridized electrochemically reduced graphene oxide; MWCNTs: multiple-wall carbon nanotubes; CS: chitosan; CdS: cadmium sulfide.

4. Conclusions

In this study, we synthesized a novel Bi_2MoO_6 nanohybrid with a tremella-like structure by doping Mo into Bi_2O_3. The combination of Bi with Mo led to the change of the morphology from sphere to tremella with a larger surface area and obvious enhancement in the conductivity due to the synergistic effects of Bi and Mo. After being decorated with Au NPs, both the conductivity and biocompatibility of the synthesized Au@Bi_2MoO_6 NTs were further improved, and thus used as an electrochemical immunosensing platform to detect CEA. The proposed immunosensor exhibited promising analytical performance toward CEA in a wide concentration range. The detection limit was comparable to that of other immunosensors for CEA detection. Moreover, both the specificity and the reproducibility of the immunosensor were qualified and superior to other materials in terms of biocompatibility, showing a great prospect in clinical CEA detection.

Conflicts of interest

There is no conflict of interest in this work.

Acknowledgements

This work was financially supported by the Shanghai Natural Science Foundation (19ZR1434800 and 19ZR1461900). The authors greatly appreciate these supports.

References

1 P. A. Crosbie, R. Shah, Y. Summers, C. Dive and F. Blackhall, Prognostic and predictive biomarkers in early stage NSCLC: CTCs and serum/plasma markers, *Transl. Lung Cancer Res.*, 2013, **2**(5), 382–397.

2 Y. W. Xu, Y. H. Peng, B. Chen, Z. Y. Wu, J. Y. Wu, J. H. Shen, *et al.*, Autoantibodies as potential biomarkers for the early detection of esophageal squamous cell carcinoma, *Am. J. Gastroenterol.*, 2014, **109**(1), 36–45.

3 L. Zhao, M. Cheng, G. Liu, H. Lu, Y. Gao, X. Yan, *et al.*, A fluorescent biosensor based on molybdenum disulfide nanosheets and protein aptamer for sensitive detection of carcinoembryonic antigen, *Sens. Actuators, B*, 2018, **273**, 185–190.

4 L. A. Torre, R. L. Siegel, E. M. Ward and A. Jemal, Global Cancer Incidence and Mortality Rates and Trends–An Update, *Cancer Epidemiol., Biomarkers Prev.*, 2016, **25**(1), 16–27.

5 A. B. Chinen, C. M. Guan, J. R. Ferrer, S. N. Barnaby, T. J. Merkel and C. A. Mirkin, Nanoparticle Probes for the Detection of Cancer Biomarkers, Cells, and Tissues by Fluorescence, *Chem. Rev.*, 2015, **115**(19), 10530–10574.

6 F. Y. Kong, B. Y. Xu, Y. Du, J. J. Xu and H. Y. Chen, A branched electrode based electrochemical platform: towards new label-free and reagentless simultaneous detection of two biomarkers, *Chem. Commun.*, 2013, **49**(11), 1052–1054.

7 Y. S. Gao, X. F. Zhu, J. K. Xu, L. M. Lu, W. M. Wang, T. T. Yang, *et al.*, Label-free electrochemical immunosensor based on Nile blue A-reduced graphene oxide nanocomposites for carcinoembryonic antigen detection, *Anal. Biochem.*, 2016, **500**, 80–87.

8 W.-T. Li, Y. Wang, F.-F. Deng, L.-L. Liu, H.-J. Nan and H. Li, Electrochemical Immunosensor for Carcinoembryonic Antigen Detection Based on Mo-Mn_3O_4/MWCNTs/Chits Nanocomposite Modified ITO Electrode, *Nanotechnology*, 2015, **10**(8), 1550111.

9 A. P. Yang, J. Liu, H. Y. Lei, Q. W. Zhang, L. Zhao and G. H. Yang, CA72-4 combined with CEA, CA125 and CAl9-9 improves the sensitivity for the early diagnosis of gastric cancer, *Clin. Chim. Acta*, 2014, **437**, 183–186.

10 C. Aggarwal, N. J. Meropol, C. J. Punt, N. Iannotti, B. H. Saidman, K. D. Sabbath, *et al.*, Relationship among circulating tumor cells, CEA and overall survival in patients with metastatic colorectal cancer, *Ann. Oncol.*, 2013, **24**(2), 420–428.

11 P. Yanez-Sedeno, S. Campuzano and J. M. Pingarron, Multiplexed Electrochemical Immunosensors for Clinical Biomarkers, *Sensors*, 2017, **17**(5), 965.

12 W. Shi and Z. Ma, A novel label-free amperometric immunosensor for carcinoembryonic antigen based on redox membrane, *Biosens. Bioelectron.*, 2011, **26**(6), 3068–3071.

13 H. Li, J. He, S. Li and A. P. Turner, Electrochemical immunosensor with N-doped graphene-modified electrode for label-free detection of the breast cancer biomarker CA 15-3, *Biosens. Bioelectron.*, 2013, **43**, 25–29.

14 L. Li, B. Liang, F. Li, J. Shi, M. Mascini, Q. Lang, *et al.*, Co-immobilization of glucose oxidase and xylose dehydrogenase displayed whole cell on multiwalled carbon nanotube nanocomposite films modified electrode for simultaneous voltammetric detection of D-glucose and D-xylose, *Biosens. Bioelectron.*, 2013, **42**, 156–162.

15 L.-B. Zhang, S.-R. Yang, J.-Q. Wang, Y. Xu and X.-Z. Kong, A facile preparation and electrochemical properties of nickel based compound–graphene sheet composites for supercapacitors, *Chin. Chem. Lett.*, 2015, **26**(5), 522–528.

16 Z. Qiu, J. Shu and D. Tang, Bioresponsive Release System for Visual Fluorescence Detection of Carcinoembryonic Antigen from Mesoporous Silica Nanocontainers Mediated Optical Color on Quantum Dot-Enzyme-Impregnated Paper, *Anal. Chem.*, 2017, **89**(9), 5152–5160.

17 G. Nie, Y. Tang, B. Zhang, Y. Wang and Q. Guo, Label-free photoelectrochemical immunosensing platform for detection of carcinoembryonic antigen through photoactive conducting poly(5-formylindole) nanocomposite, *Biosens. Bioelectron.*, 2018, **116**, 60–66.

18 S. Kumar, M. Umar, A. Saifi, S. Kumar, S. Augustine, S. Srivastava, *et al.*, Electrochemical paper based cancer biosensor using iron oxide nanoparticles decorated PEDOT:PSS, *Anal. Chim. Acta*, 2019, **1056**, 135–145.

19 X. Zhang, N. Bao, X. Luo and S. N. Ding, Patchy gold coated Fe_3O_4 nanospheres with enhanced catalytic activity applied for paper-based bipolar electrode-electrochemiluminescence aptasensors, *Biosens. Bioelectron.*, 2018, **114**, 44–51.

20 P. D. Tam and C. X. Thang, Label-free electrochemical immunosensor based on cerium oxide nanowires for Vibrio cholerae O1 detection, *Mater. Sci. Eng., C*, 2016, **58**, 953–959.

21 F. Li, Y. Li, J. Feng, Y. Dong, P. Wang, L. Chen, *et al.*, Ultrasensitive amperometric immunosensor for PSA detection based on Cu_2O@CeO_2-Au nanocomposites as integrated triple signal amplification strategy, *Biosens. Bioelectron.*, 2017, **87**, 630–637.

22 M. Li, P. Wang, F. Li, Q. Chu, Y. Li and Y. Dong, An ultrasensitive sandwich-type electrochemical immunosensor based on the signal amplification strategy of mesoporous core-shell Pd@Pt nanoparticles/amino group functionalized graphene nanocomposite, *Biosens. Bioelectron.*, 2017, **87**, 752–759.

23 R. Jain and R. Sharma, Novel bismuth/multi-walled carbon nanotubes-based electrochemical sensor for the determination of neuroprotective drug cilostazol, *J. Appl. Electrochem.*, 2012, **42**(5), 341–348.

24 Y. Chen, P.-X. Yuan, A.-J. Wang, X. Luo, Y. Xue and L. Zhang, A novel electrochemical immunosensor for highly sensitive detection of prostate-specific antigen using 3D open-structured PtCu nanoframes for signal amplification, *Biosens. Bioelelctron.*, 2019, **126**, 187–192.

25 Q. Han, R. Wang, B. Xing, H. Chi, D. Wu and Q. Wei, Label-free photoelectrochemical aptasensor for tetracycline detection based on cerium doped CdS sensitized $BiYWO_6$, *Biosens. Bioelelctron.*, 2018, **106**, 7–13.

26 Q. Han, H. Chi, H. Wang, D. Wu and Q. Wei, Using PbS-Au heterodimers as signal quencher for the sensitive photoelectrochemical immunoassay of amyloid β-protein, *Anal. Chim. Acta*, 2019, **1092**, 85–92.

27 J. Feng, Y. Li, Z. Gao, H. Lv, X. Zhang, Y. Dong, *et al.*, A competitive-type photoelectrochemical immunosensor for aflatoxin B1 detection based on flower-like WO_3 as matrix and Ag_2 S-enhanced BiVO 4 for signal amplification, *Sens. Actuators, B*, 2018, **270**, 104–111.

28 Y. Qiu, H. Fan, X. Chang, H. Dang, Q. Luo and Z. Cheng, Novel ultrathin Bi2O3 nanowires for supercapacitor electrode materials with high performance, *Appl. Surf. Sci.*, 2018, **434**, 16–20.

29 J. Hu, G. Xu, J. Wang, J. Lv, X. Zhang, T. Xie, *et al.*, Photocatalytic property of a Bi_2O_3 nanoparticle modified BiOCl composite with a nanolayered hierarchical structure synthesized by *in situ* reactions, *Dalton Trans.*, 2015, **44**(12), 5386–5395.

30 S. N. Ding, D. Shan, H.-G. Xue and S. C. J. Bioelectrochemistry, A promising biosensing-platform based on bismuth oxide polycrystalline-modified electrode: characterization and its application in development of amperometric glucose sensor, *Bioelectrochemistry*, 2010, **79**(2), 218–222.

31 P. R. Solanki, J. Singh, B. Rupavali, S. Tiwari and B. D. Malhotra, Bismuth oxide nanorods based immunosensor for mycotoxin detection, *Mater. Sci. Eng., C*, 2016, **70**, 564–571.

32 Z. Gao, Y. Li, C. Zhang, S. Zhang, F. Li, P. Wang, *et al.*, Label-free electrochemical immunosensor for insulin detection by high-efficiency synergy strategy of Pd NPs@3D MoS_x towards H_2O_2, *Biosens. Bioelectron.*, 2019, **126**, 108–114.

33 B. Zhang, Y. Xue, A. Jiang, Z. Xue, Z. Li and J. Hao, Ionic Liquid as Reaction Medium for Synthesis of Hierarchically Structured One-Dimensional MoO_2 for Efficient Hydrogen Evolution, *ACS Appl. Mater. Interfaces*, 2017, **9**(8), 7217–7223.

34 F. Li, Y. Li, J. Feng, Z. Gao, H. Lv, X. Ren, *et al.*, Facile synthesis of MoS_2@Cu_2O-Pt nanohybrid as enzyme-mimetic label for the detection of the Hepatitis B surface antigen, *Biosens. Bioelectron.*, 2018, **100**, 512–518.

35 Z. Gao, Y. Li, X. Zhang, J. Feng, L. Kong, P. Wang, *et al.*, Ultrasensitive electrochemical immunosensor for quantitative detection of HBeAg using Au@Pd/MoS_2@MWCNTs nanocomposite as enzyme-mimetic labels, *Biosens. Bioelectron.*, 2018, **102**, 189–195.

36 Z. Li, Y. Hu, Z. Miao, H. Xu, C. Li, Y. Zhao, *et al.*, Dual-Stimuli Responsive Bismuth Nanoraspberries for Multimodal Imaging and Combined Cancer Therapy, *Nano Lett.*, 2018, **18**(11), 6778–6788.

37 W. Liu, X. Li, W. Li, Q. Zhang, H. Bai, J. Li, *et al.*, Highly stable molybdenum dioxide nanoparticles with strong plasmon resonance are promising in photothermal cancer therapy, *Biomaterials*, 2018, **163**, 43–54.

38 Q. Yan, L. Cao, H. Dong, Z. Tan, Y. Hu, Q. Liu, *et al.*, Label-free immunosensors based on a novel multi-amplification signal strategy of TiO_2-NGO/Au@Pd hetero-nanostructures, *Biosens. Bioelectron.*, 2019, **127**, 174–180.

39 J. C. Jung, H. Lee, H. Kim, Y.-M. Chung, T. J. Kim, S. J. Lee, *et al.*, Effect of Oxygen Capacity and Oxygen Mobility of Pure Bismuth Molybdate and Multicomponent Bismuth Molybdate on their Catalytic Performance in the Oxidative Dehydrogenation of n-Butene to 1,3-Butadiene, *Catal. Lett.*, 2008, **124**(3–4), 262–267.

40 B. Kavosi, A. Salimi, R. Hallaj and F. Moradi, Ultrasensitive electrochemical immunosensor for PSA biomarker detection in prostate cancer cells using gold nanoparticles/PAMAM dendrimer loaded with enzyme linked aptamer as integrated triple signal amplification strategy, *Biosens. Bioelectron.*, 2015, **74**, 915–923.

41 D. T. Tran, V. H. Hoa, L. H. Tuan, N. H. Kim and J. H. Lee, Cu-Au nanocrystals functionalized carbon nanotube arrays vertically grown on carbon spheres for highly sensitive detecting cancer biomarker, *Biosens. Bioelectron.*, 2018, **119**, 134–140.

42 J. Liu, J. Wang, T. Wang, D. Li, F. Xi, J. Wang, *et al.*, Three-dimensional electrochemical immunosensor for sensitive detection of carcinoembryonic antigen based on monolithic and macroporous graphene foam, *Biosens. Bioelectron.*, 2015, **65**, 281–286.

43 N. Alizadeh, A. Salimi and R. Hallaj, Mimicking peroxidase activity of $Co_2(OH)_2CO_3$-CeO_2 nanocomposite for smartphone based detection of tumor marker using paper-based microfluidic immunodevice, *Talanta*, 2018, **189**, 100–110.

44 L. Chen, X. Zeng, P. Si, Y. Chen, Y. Chi, D. H. Kim, *et al.*, Gold nanoparticle-graphite-like C_3N_4 nanosheet nanohybrids used for electrochemiluminescent immunosensor, *Anal. Chem.*, 2014, **86**(9), 4188–4195.

45 K. Huang, Z. Wu, Y. Wu and Y. Liu, Electrochemical immunoassay of carcinoembryonic antigen based on TiO_2–graphene/thionine/gold nanoparticles composite, *Can. J. Chem.*, 2012, **90**(7), 608–615.

46 Y. Zhuo, P. X. Yuan, R. Yuan, Y. Q. Chai and C. L. Hong, Bienzyme functionalized three-layer composite magnetic nanoparticles for electrochemical immunosensors, *Biomaterials*, 2009, **30**(12), 2284–2290.

47 K. J. Huang, D. J. Niu, W. Z. Xie and W. Wang, A disposable electrochemical immunosensor for carcinoembryonic antigen based on nano-Au/multi-walled carbon nanotubes-chitosans nanocomposite film modified glassy carbon electrode, *Anal. Chim. Acta*, 2010, **659**(1–2), 102–108.

48 L. Zhao, M. Cheng, G. Liu, H. Lu, Y. Gao, X. Yan, *et al.*, A fluorescent biosensor based on molybdenum disulfide nanosheets and protein aptamer for sensitive detection of carcinoembryonic antigen, *Sens. Actuators, B*, 2018, **273**, 185–190.

49 H. Wang, B. Zhang, J. Xi, F. Zhao and B. Zeng, Z-scheme I-BiOCl/CdS with abundant oxygen vacancies as highly effective cathodic material for photocathodic immunoassay, *Biosens. Bioelectron.*, 2019, **141**, 111443.

